

Molecular Modeling of the Dissociation of Methane Hydrate in Contact with a Silica Surface

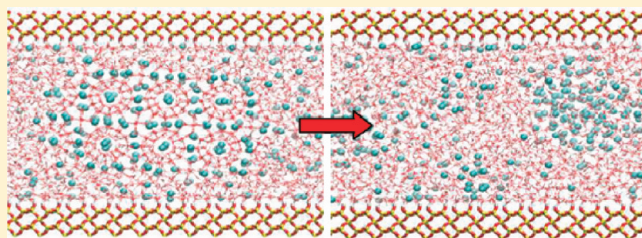
S. Alireza Bagherzadeh,[†] Peter Englezos,^{*,†} Saman Alavi,^{*,‡} and John A. Ripmeester^{*,‡}

[†]Department of Chemical and Biological Engineering, University of British Columbia, Vancouver, British Columbia, V6T 1Z3, Canada

[‡]Steacie Institute for Molecular Sciences, National Research Council of Canada, Ottawa, Ontario, K1A 0R6, Canada

Supporting Information

ABSTRACT: We use constant energy, constant volume (*NVE*) molecular dynamics simulations to study the dissociation of the fully occupied structure I methane hydrate in a confined geometry between two hydroxylated silica surfaces between 36 and 41 Å apart, at initial temperatures of 283, 293, and 303 K. Simulations of the two-phase hydrate/water system are performed in the presence of silica, with and without a 3 Å thick buffering water layer between the hydrate phase and silica surfaces. Faster decomposition is observed in the presence of silica, where the hydrate phase is prone to decomposition from four surfaces, as compared to only two sides in the case of the hydrate/water simulations. The existence of the water layer between the hydrate phase and the silica surface stabilizes the hydrate phase relative to the case where the hydrate is in direct contact with silica. Hydrates bound between the silica surfaces dissociate layer-by-layer in a shrinking core manner with a curved decomposition front which extends over a 5–8 Å thickness. Labeling water molecules shows that there is exchange of water molecules between the surrounding liquid and intact cages in the methane hydrate phase. In all cases, decomposition of the methane hydrate phase led to the formation of methane nanobubbles in the liquid water phase.



1. INTRODUCTION

After the discovery of synthetic and natural hydrates,^{1–5} it was realized that this unconventional source of methane and natural gas can potentially serve as an energy source for the future.^{6–8} The global estimate of methane stored in hydrates under the ocean floor and permafrost falls in the range from 1×10^{15} to $1.2 \times 10^{17} \text{ m}^3$ at standard conditions.⁷ However, the challenge is to find safe, controllable, and economical strategies to exploit the gas from these vast reserves. So far, depressurization, thermal stimulation, inhibitor injection,⁶ and guest exchange⁹ have been proposed as gas extraction techniques.

Hydrates usually occur in natural porous environments such as permafrost and sea floor sediments. Hence, in order to understand the formation and dissociation of hydrates in nature, it is essential to investigate these processes in porous media. Molecular dynamics (MD) simulations of the dissociation of methane hydrate in contact with water phase have been widely performed^{10–27} and discussed in detail in our previous publications.^{24,28} These simulations are usually performed under the operation of a MD thermostat at an “over-temperature” higher than the hydrate–water–gas equilibrium points. The setup of the simulation usually includes the hydrate phase in contact with bulk water. We recently performed molecular dynamics simulations on methane hydrate dissociation under adiabatic, constant energy, constant volume (*NVE*) conditions.^{24,28} The heat consumed during hydrate dissociation and the heat transfer from the liquid to the hydrate

phase were found to play important roles in the mechanism and rate of the decomposition. It was noted that in isothermal MD simulations, the thermostats remove or provide “heat” to the system (by scaling the velocities of the molecules to impose the constant temperature condition) and cannot sustain heat transfer, particularly for the size and time scales of the MD simulations of methane hydrate. We believe that the temperature and mass gradients play important roles in methane hydrate dissociation under experimental conditions. Even if methane hydrate decomposition occurs in a stirred reactor, nanoscale thermal gradients at the hydrate surface will still persist due to nonslip boundary conditions, and therefore, the overall decomposition kinetics will depend on the heat and mass transfer.

Understanding the details of methane hydrate dissociation, especially in porous media and under restricted geometry, can be beneficial in designing optimal processes for CH_4 extraction from natural methane hydrate reservoirs. Since it is known that sandy environments contain the highest hydrate saturation,²⁹ we incorporate silica in our simulations to investigate the effect of specific hydrate–water–silica interactions and the effect of restricted geometry on the hydrate dissociation behavior.

Received: September 8, 2011

Revised: February 23, 2012

Published: February 27, 2012

Recently, Bai et al.³⁰ conducted constant pressure, constant temperature (*NPT*) MD simulations to determine the heterogeneous nucleation mechanism of the formation of CO₂ hydrate in the presence of hydroxylated silica surfaces. They observed the presence of relatively immobile layers of water molecules adjacent to the silica surfaces which persist even after CO₂ structure I (sI) hydrate is formed in the simulation cell. In other words, solid hydrate does not form in direct contact with the hydroxylated silica surface. In their simulation, due to the high solubility of CO₂ in water, there is no CO₂ gas separation from the aqueous phase. This is in contrast to methane gas, which has very low solubility in water and as a result hydrate formation on a silica surface will likely be a three-phase solid–liquid–gas process. Liang et al.³¹ found that methane hydrate growth in bulk solution (away from the silica surfaces) proceeds ahead of that adjacent the silica surface. Additionally, a layer of water with a thickness of about 5 Å near the hydroxylated silica surface was observed to have different characteristics from that of bulk water.

In this paper, we study the dissociation of methane hydrate in contact with a hydroxylated silica surface with *NVE* MD simulations starting at different initial temperatures. Three sets of simulations are performed. In the first set, we simulate methane hydrate decomposition in contact with water as the reference system. In the next two series of simulations, we perform simulations of methane hydrate in contact with water on two sides (in the *z*-direction) and having interfacial contact with hydroxylated silica on two other surfaces (in the *y*-direction). One set of simulations has the solid methane hydrate phase in direct contact with the hydroxylated silica surfaces, and the other set of simulations has a relatively thin layer of water (3 Å) acting as a buffer between the hydroxylated silica and methane hydrate surface to relieve the mismatch between these two solid lattices. We are interested in studying the effect of the silica surface on the decomposition of methane hydrate as a first step in understanding hydrate dissociation under conditions closer to the experimental conditions. By performing *NVE* simulations, we account for the endothermic nature of the hydrate dissociation and allow for the formation of temperature gradients between the decomposing hydrate surface and the bulk water phase.

A MD setup for the simulations of methane hydrate dissociation in the presence of the silica surface that is closer to the experimental conditions would be to have two large thermostated water reservoirs (both at the same target temperature and pressure) in contact with nonthermostated water reservoirs (adiabatic *NVE*) at a temperature T_{water} , which are then in contact with the nonthermostated (adiabatic *NVE*) hydrate phase at an initial equilibrium temperature of $T_{\text{hydrate}} < T_{\text{water}}$. The heat conductance between the water and hydrate phase in this setup would more accurately represent the experimental setup for the hydrate melting. Performing the simulation in this manner would be feasible, but we believe the simpler *NVE* simulations of the present work are useful for illustrating the general features of the hydrate dissociation process.

The paper is organized as follows. In the next section, the simulation protocol, force fields, and initial configurations, as well as the methods used for analyzing the results, are given. The results are discussed in the following section and paper ends with the conclusions.

2. COMPUTATIONAL METHODS

The molecular dynamics (MD) simulations were run with the DL_POLY program (version 2.20).³² The intermolecular potential for atoms on different molecules is considered as a sum of Lennard-Jones and Columbic interactions, with force field parameters summarized in Table 1. A united-atom

Table 1. Lennard-Jones Potential Parameters and Partial Atomic Charges^a

atom	ϵ (kJ·mol ⁻¹)	σ (Å)	q (e)
CH ₄	1.3650	3.6400	
O (H ₂ O)	0.6502	3.166	-0.8476
H (H ₂ O)			+0.4238
Si (SiO ₂ bulk)	2.5104	3.9200	+1.08
O (SiO ₂ bulk)	0.6364	3.1538	-0.53
O (SiO ₂ surface)	0.6364	3.1538	-0.64
H (SiO ₂ surface)	0.1925	0.4000	+0.32

^aThe united atom model was applied for methane,³³ the SPC/E model for water,³⁴ and the empirical force field of Lopes et al.³⁵ for silica.

potential was used for methane,³³ the SPC/E potential for water,³⁴ and the potential of Lopes et al.³⁵ for the silica atomic interactions. Standard combination rules were used to calculate the Lennard-Jones parameters for the unlike pairs of atoms, $\epsilon_{ij} = (\epsilon_{ii}\epsilon_{jj})^{1/2}$ and $\sigma_{ij} = (\sigma_{ii} + \sigma_{jj})/2$. The cutoff radius for all of interatomic interactions in the simulation box is set to 15 Å and the long-range Columbic interactions were treated using the Ewald summation method. Periodic boundary conditions are applied in all three dimensions.

The orthorhombic repeating unit for silica (quartz) was extracted from the crystallographic hexagonal unit cell of this substance available at the American Mineralogist Crystal Structure Database.³⁶ The unit cell parameters and other details for the construction of this repeat unit are given in the Supporting Information. The layer of silicon atoms of the silica phase in contact with water and the methane hydrate phase are hydrated with OH groups with an O–H bond length of 1.1 Å, as suggested by Lopes et al.³⁵ The atoms of the silica slabs were kept frozen during the simulations and therefore do not participate in heat transfer.

As a reference system, a $3 \times 3 \times 6$ unit cell replica of the cubic sI hydrate ($a = 11.94$ Å) was prepared with methane molecules placed at the center of the small and large cages. A row of water and methane molecules were eliminated from one end of the hydrate phase in the *z*-direction to render the hydrate phase symmetric along this direction. A total of 2322 water and 357 methane molecules were present in the initial methane hydrate phase. Two reservoirs of water (a total of 5406 water molecules) were added to both sides of the hydrate phase along the *z*-direction such that the lengths of these water reservoirs on each side were approximately half the size of the hydrate phase. This arrangement is called the *hydrate–water (HW) scenario*. The initial configuration of the system is shown in Figure 1a. To equilibrate the system and relax the water molecules at the hydrate/water interface, 400 ps constant volume–constant temperature (*NVT*) runs were performed followed by 400 ps *NPT* simulations for pressure relaxation. Thermostat and barostat constants of 0.2 and 0.5 ps were used in these simulations. During both of these simulations, the hydrate phase was frozen to prevent decomposition. The hydrate phase was allowed to dissociate in a final 2 ns *NVE* simulation. Using these protocols three sets of simulations were

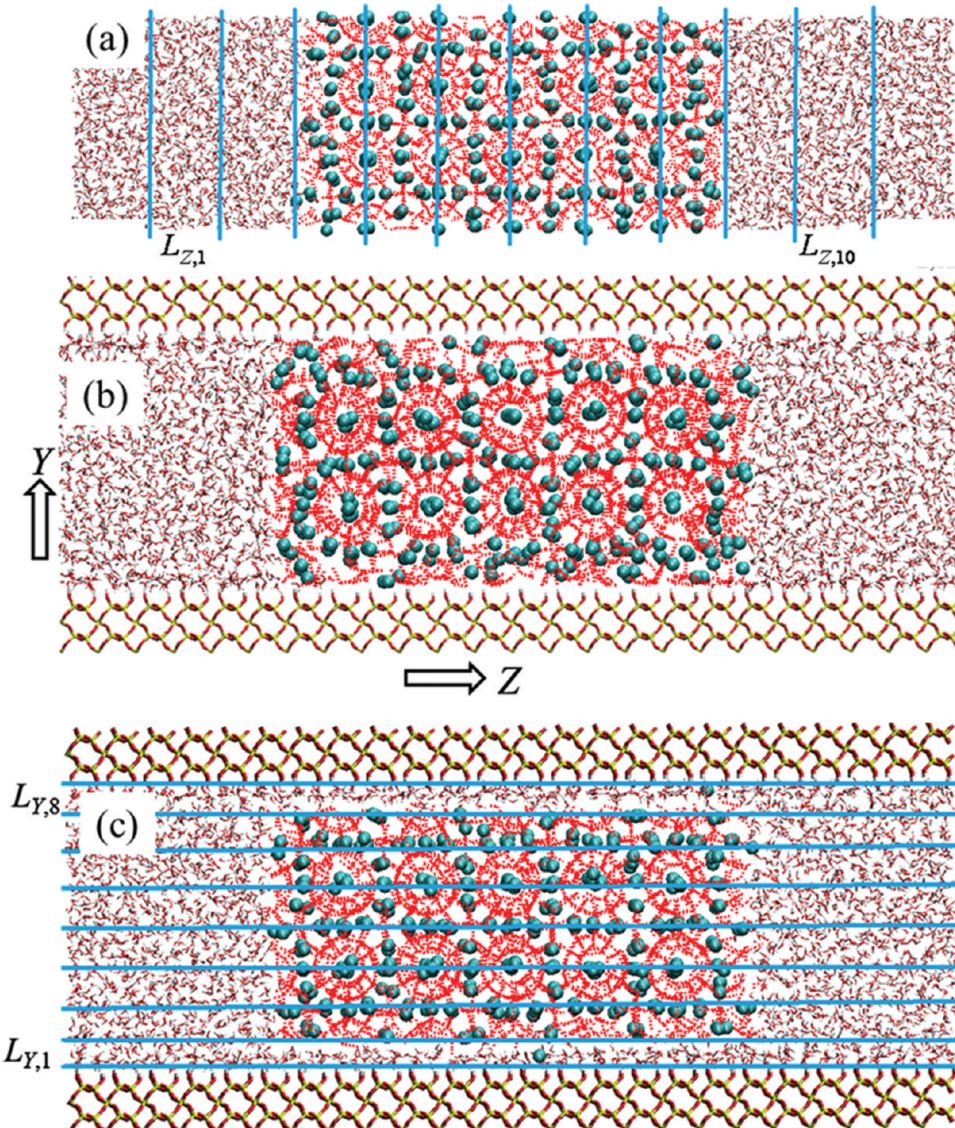


Figure 1. The initial configurations for simulation of methane hydrate dissociation: (a) HW scenario, (b) SHW scenario, and (c) SWHW scenario. The 10 slabs perpendicular to the z -direction and 6 and 8 slabs perpendicular to the y -direction used to characterize the system behavior during methane hydrate dissociation are also shown. For clarity, binning is only illustrated along the z -direction in HW scenario and along the y -direction in the SWHW scenario. The length of the simulation box along the z -direction is $L_z = 145 \text{ \AA}$ and along the x -direction is $L_x = 36 \text{ \AA}$.

conducted with initial temperatures of 283, 293, and 303 K. The final pressure in the three HW simulations converged to about 0.8 kbar. A time step of 1 fs was used in all of the simulations.

For simulations of methane hydrate decomposition in the presence of the silica surface, two scenarios are considered. In the first scenario, called the *silica–hydrate–water* (SHW) scenario, shown in Figure 1b, the methane hydrate phase (of the same size and structure as used in the HW simulations) is placed in between two hydroxylated silica surfaces separated by 36.6 Å, with the two phases separated by the van der Waals radii. A total of 2670 water molecules are placed outside the methane hydrate phase, in between the silica surfaces. In the second case, called the *silica–water–hydrate–water* (SWHW) scenario, shown in Figure 1c, the silica layers are moved further out along the y -direction and a $\sim 3 \text{ \AA}$ layer of water is placed in between the methane hydrate and the silica surfaces. There are a total of 3413 water molecules in the initial liquid phase in this setup. The details of the structure of the hydroxylated silica

layers are given in the Supporting Information. It is known that water in porous media forms a thin layer, called the “bound water”, which attaches to pore walls and does not undergo a melting/freezing phase change.^{39,40} Using thermoporometric analysis, Handa et al.³⁹ obtained a thickness of 4.5–5.5 Å for the bound water layer in porous silica gels with pore radii range of 23–70 Å. The SWHW scenario is meant to mimic these conditions. Three 400 ps NVT simulations at 283, 293, and 303 K with frozen hydrate phases were carried out for the SHW and SWHW system, followed by 2 ns NVE simulations, where the methane hydrate phase is allowed to dissociate. The silica phase is frozen throughout these simulations.

The F_3 order parameter of Baez and Clancy¹⁰ is used to characterize the local state of the water molecules during the hydrate decomposition simulation. The F_3 parameter is based on the 104.25° O–O–O angle observed in tetrahedral arrangement of water oxygen atoms in ice and hydrate phases. This angle provides a measure of the deviation of the hydrogen-

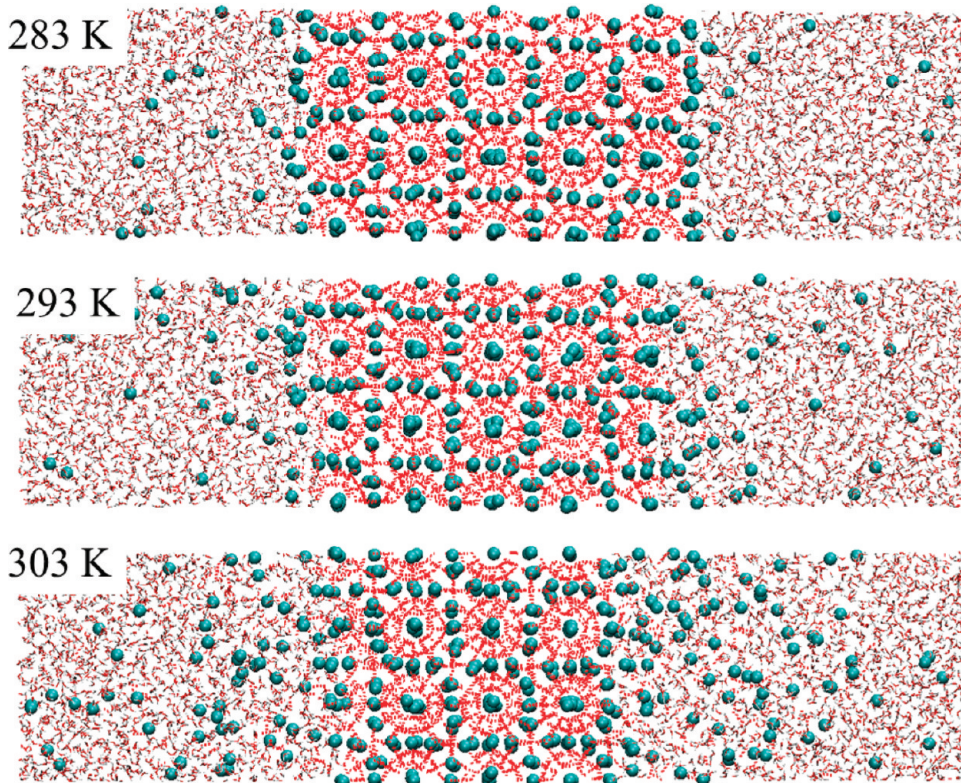


Figure 2. The configurations at the end of the 2 ns runs with $T_{\text{init}} = 283, 293$, and 303 K in the HW scenario. Methane molecules, liquid water, and hydrate are represented by cyan spheres, red-white bonds, and, red dotted hydrogen bonds, respectively.

bonding network from the ideal tetrahedral arrangement in the solid state of water,

$$F_{3,i} = \langle [\cos \theta_{jik} |\cos \theta_{jik}| + \cos^2 104.25]^2 \rangle_{j,k}$$

$$= \begin{cases} \sim 0.1 & \text{liquid water} \\ \sim 0.0 & \text{solid water (ice, hydrate)} \end{cases} \quad (2)$$

where θ_{jik} is the angle between triplets of oxygen atoms with the i th atom being in the center. The j and k oxygen atoms are within a spherical shell of radius 3.5 Å around atom i (the first peak in the radial distribution function of O–O pairs of water molecules in liquid water phase).

To analyze the structure of the phases, the simulation cell is subdivided into 10 layers in the z -direction, each ~ 12 Å in thickness, as shown in Figure 1a. The order parameter can be separately averaged over all water molecules in the simulation cell, designated as F_3 , over all water molecules initially in the hydrate phase, $F_{3,\text{hydrate}}$ or only over water molecules within the i th layer perpendicular to the z -axis, F_{3,L_i} . The decomposition of methane hydrate is associated with the increase of the F_3 value from ~ 0.0 to ~ 0.1 . We also study the variation of the F_3 order parameters in eight layers in the y -direction to study the methane hydrate decomposition parallel to the silica surface; see Figure 1c.

The potentials used in the simulation have not been calibrated against the methane hydrate dissociation curve and so the temperature/pressure values of the simulations may be shifted with respect to the experimental phase diagram. Although the absolute values of the pressure and temperature of the phase transformations may differ from the experimental values, the trends are quantitatively reasonable.

Previous simulation studies of the methane hydrate decomposition temperature for the SPC/E, TIP4P, and TIPSP water potentials and a five-site potential for methane have been performed by Luis et al.³⁷ At a pressure of 20 atm, they observe that the predicted decomposition temperature of ~ 280 K for the SPC/E is closer to the experimental value of 268 K (at 20 atm) than the TIP4P and TIPSP predicted results. On the basis of these simulation results, we expect the simulation at 283 K to be near the methane clathrate hydrate decomposition (melting) temperature for the choice of the potentials used in these simulations and the simulations at 293 and 303 K to be superheated. The triple point of methane hydrate with water and methane has also been studied computationally for TIP4P water potentials and a single Lennard-Jones site potential for methane.³⁸

3. RESULTS AND DISCUSSION

The configurations of the water–hydrate systems with three different initial temperatures at the end of the NVE simulations for the HW scenario are given in Figure 2. The hydrate has not decomposed to an appreciable extent in the simulations with $T_{\text{init}} = 283$ and 293 K. The evolution of the local structures of the phases in the HW simulation with $T_{\text{init}} = 283$ K are shown in Figure 3 by calculating the local water order parameters F_{3,L_i} for layers in the simulation perpendicular to the z -direction. In Figure 3, the layers at the methane hydrate/water interface (L_3 and L_8 , green and violet lines) which contain water molecules from both hydrate phase and liquid phases, have order parameters ($F_3 \approx 0.04$) between that of the solid methane hydrate ($F_3 \approx 0.02$) and liquid water ($F_3 \approx 0.1$) values. There is a small amount of hydrate dissociation at these layers since F_{3,L_i} increases slightly with time. In the HW scenario for $T_{\text{init}} = 293$

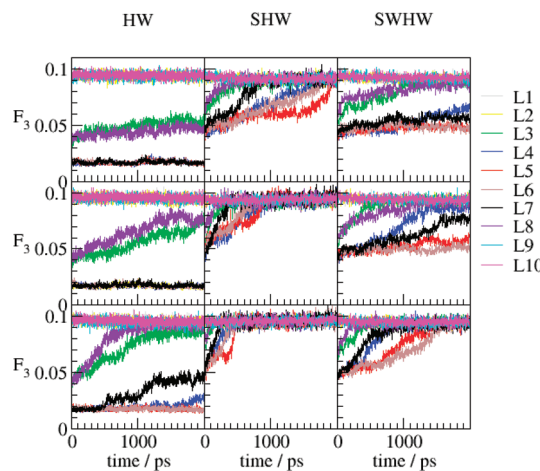


Figure 3. The F_{3,L_i} order parameter for the water and hydrate phases as a function of time for different layers perpendicular the z -direction (see Figure 1) for simulations with $T_{\text{init}} = 283$ (top row), 293 (middle row), and 303 K (bottom row). In the HW scenario at 283 K, no large scale dissociation of the methane hydrate phase occurs and the incomplete cages at the interface (slabs 3 and 8), show F_{3,L_i} values of 0.04, which are between the hydrate-like and liquid-like states of water.

and 303 K, by the end of the 2 ns simulation, the outmost L_3 and L_8 layers of the methane hydrate phase have become liquid ($F_3 \approx 0.1$). For the $T_{\text{init}} = 293$ K simulation, L_3 and L_8 are the only two layers that have dissociated to an appreciable extent. The stepwise dissociation of the hydrate phase at $T_{\text{init}} = 303$ K is apparent. The outmost L_3 and L_8 layers at the methane hydrate/water interface dissociate first. After these layers have substantially dissociated, as characterized by $F_{3,L_i} \approx 0.08$, the decomposition of the next inner layers (L_4 and L_7 , blue and black, respectively) begins.

For the set of potential energy functions chosen for this work, the F_3 values for the different layers indicate that the methane hydrate/water system equilibrium temperature is near 283 K.

The changes in the local structure of phases for the SHW and SWHW scenarios for $T_{\text{init}} = 283, 293$, and 303 K are also shown in Figure 3. The higher starting values of the F_3 parameter ($F_3 \approx 0.05$) for the SWHW and SHW scenarios at $t = 0$ are due to the quick decomposition of the hydrate phase adjacent to the silica surface. It is clear that decomposition under HW conditions proceeds through the decomposition of rows of hydrate cages parallel to the interface and the dissociation front is relatively well-defined, a phenomenon reported in earlier studies.^{3,18,24} The F_3 curves in Figure 3 (particularly for the SWHW scenario) show that the dissociation of methane hydrate in the presence of silica interfaces still proceeds in a stepwise manner with outer layers decomposing before inner layers. However, due to the effects of the additional boundaries, the methane hydrate also dissociates from the sides in contact with the silica surface, and therefore, decomposition of each layer perpendicular to the z -direction does not proceed as clearly defined as in the HW case.

The time variation of the temperature profiles of the entire simulation cell are shown in Figure 4. The decomposition of methane hydrate is endothermic, and as the simulations progresses, the average temperature in the NVE simulation drops. Due to the greater extent of methane hydrate decomposition, the temperature drop for the SWHW and

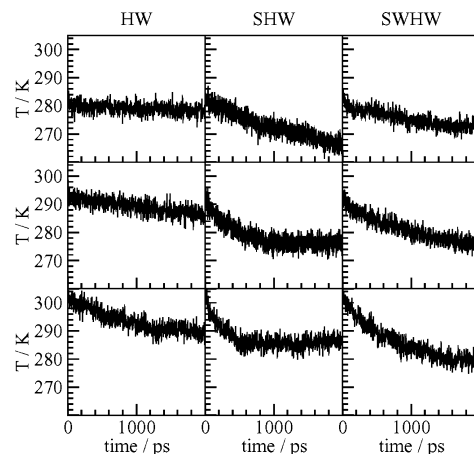


Figure 4. Temperature profiles for the simulations at 283 K (top), 293 K (middle), and 303 K (bottom) in the NVE ensemble for three different scenarios introduced in the text: HW (left), SHW (middle), and SWHW (right). The drop in temperature is an indication of hydrate dissociation.

SHW simulations in the presence of hydroxylated silica are higher than those of the HW scenario. Temperature drops as large as ~ 20 K are observed in the SWHW scenario at 303 K. The variations in the pressure of the systems are given in the Supporting Information.

For the HW scenario at 303 K, as a result of the endothermic hydrate decomposition, the temperature drops to ~ 290 K at 1.3 ns, and after this time, hydrate decomposition effectively ceases. Since the simulations are adiabatic, as a consequence of the decrease in temperature, the rate of decomposition of the remaining methane hydrate phase and the rate of further temperature drop decreases. This is known to be a problem in naturally occurring methane hydrate reservoirs, where the depressurization technique is employed to extract methane from the hydrate deposits without supplying the heat required for the endothermic reaction of hydrate decomposition.

Some of the temperature plots in Figure 4 do not have clear temperature plateaus. This shows that the corresponding simulations have not reached equilibrium. Our goal in this work is not to continue these nonequilibrium simulations until they reached a final equilibrium state, but rather to use the evolving temperature as a measure of the rate of hydrate dissociation. The simulations would all either reach equilibrium at the hydrate melting point between hydrate and water phases or proceed until all the hydrate is dissociated and the system consists of water and methane gas.

There is an associated increase in pressure with hydrate dissociation, as shown in Figure S3 of the Supporting Information. The mismatch between the interfaces of the methane hydrate and hydroxylated silica surfaces in the absence of the liquid bound water layer between them may lead to tension between these two phases, and as a result, the absolute values of the calculated pressures may not be accurate. However, changes in pressure as the hydrate dissociates and methane is released in the simulation cell are accurately characterized. Since the methane hydrate phase decomposes to a larger extent, the pressure increase for the simulations in the presence of silica is larger than those of the HW scenario.

Interesting microscopic details are revealed by studying the hydrate/water interface for the $T_{\text{init}} = 283$ K HW simulation at different times, as shown in Figure 5. At the start of the

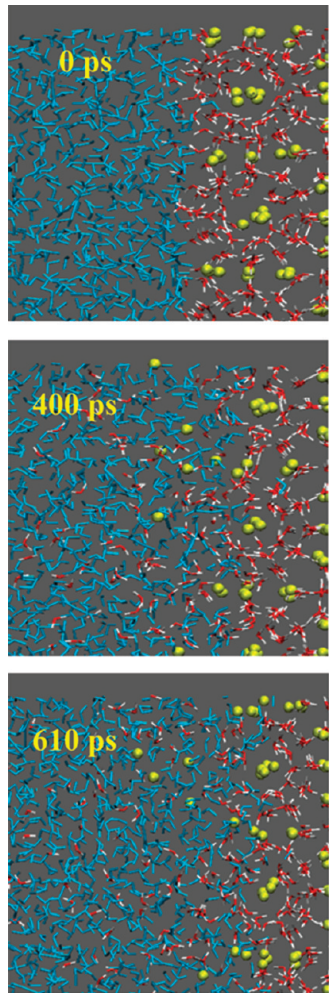


Figure 5. Snapshots of the NVE simulation of the HW scenario with methane hydrate (water molecules colored red and white) in contact with liquid water (water molecules colored blue) at 283 K. Some distortion in the methane hydrate phase and exchange of water molecules between the liquid phase and intact methane hydrate cages is observed.

simulation, the blue color-coded water molecules represent water in the liquid phase and red color-coded water molecules are in the methane hydrate phase. The same color-coding is retained for each water molecule throughout the simulation. In the three snapshots, we observe that although hydrate cages remain mainly intact, there are exchanges of water molecules between the cages and the liquid phase. The exchange of water molecules between the liquid and hydrate phases, also observed in the simulations of Walsh et al.²³ and Vatamanu et al.,⁴¹ illustrates the dynamic nature of the equilibrium between the water and hydrate phases. We speculate that temporary opening and re-forming of cages that accompanies the exchange of water molecules may provide a mechanism for guest exchange between the surrounding liquid and methane hydrate phase.

Snapshots of the configurations of the water–methane hydrate systems in the presence of silica surface with the bound water layers (SWHW scenario) at the end of the 2 ns simulations with different T_{init} values are shown in Figure 6. Methane hydrate dissociation under identical simulation conditions is much faster in these simulations than the HW simulations, as shown in Figure 3. After 2 ns, the methane

hydrate phase has completely dissociated in the simulation with $T_{\text{init}} = 303$ K and methane gas molecules have aggregated into nanobubbles.

We observe that the “bound” water molecules adjacent to the silica layer have partial ordered arrangements with hydrogen bonds to the hydroxylated silica surface; see Figure 7. This is also reported in other simulation and experimental studies.^{42–44} In the present simulations, the hydroxylated silica surface is frozen, so at least in principle, some of the order of the adjacent water molecules may be an artifact of the simulation. However, in the range of simulations temperatures, we do not expect large structural changes or atomic vibrational amplitudes in the silica surface and the water structuring will likely be seen in real systems as well. Additional simulations with flexible hydroxylated silica surfaces would be needed to verify this conclusion. The “structured” water molecules, however, are mobile and exchange with water molecules from the bulk liquid. Further analyses of the nature of the structure of the liquid water phase adjacent to the hydroxylated silica surface are in progress.

The decompositions of the methane hydrate phases in the SWHW and HW scenarios are compared by showing F_3 contours in the simulation yz -plane in Figure 8. In the SWHW simulation, the methane hydrate decomposes faster along the z -direction than the y -direction. This could be due to the restricted mobility of the water layer between the solid silica and hydrate phases in the y -direction. Moreover, it is interesting to note that the dissociation front (shown in Figure 8 by contours where F_3 changes between ~ 0.04 and ~ 0.1) is not sharp and extends over a distance of 5–8 Å in the z -direction. This predicted range of 5–8 Å over which decomposition occurs is in agreement with the reported simulation values of 10–15 Å by Rodger et al.¹³ and 5–7 Å by Myshakin et al.²² for decomposition of methane hydrate in contact with water.

The order parameter of the molecules initially in the hydrate phase, $F_{3,\text{hydrate}}$, for all of the scenarios at different temperatures is shown in Figure 9. The dissociation occurs relatively quickly in the SHW scenario with subsequent hydrate layers quickly decomposing. Furthermore, as expected, decomposition is faster at higher initial temperatures. The corresponding plots of the variation of the F_3 order parameter in the slabs along the y -direction are given in the Supporting Information (Figure S4).

In the SWHW scenario, hydrate dissociation occurs more slowly than for the SHW case, but the dissociation is faster than for the HW scenario. This is consistent with the observation that equilibrium conditions in small pores shift to higher pressures and lower temperatures, and therefore, at a specified P and T , the driving force for decomposition of methane hydrate in the pore is higher compared to the hydrate–water conditions.^{45–47} For example, Uchida et al.⁴⁸ predicted a decrease of 12.3 and 0.5 K for methane hydrate equilibrium temperature in porous glass with average pore radii of 4 and 100 nm, respectively. The enhanced rate of dissociation in the presence of the silica surface may also be a kinetic effect related to the silica surface facilitating the demixing of the methane and water of the hydrate phase through strong interactions with the water molecules.²¹ To separate the kinetic and thermodynamic aspects of methane hydrate decomposition in the presence of silica surfaces, further simulations with different slit widths need to be performed.

The formation of nanobubbles from the release of methane gas in the liquid water phase is a feature of the methane hydrate decomposition simulations. The methane bubbles formed under different simulation conditions are shown qualitatively

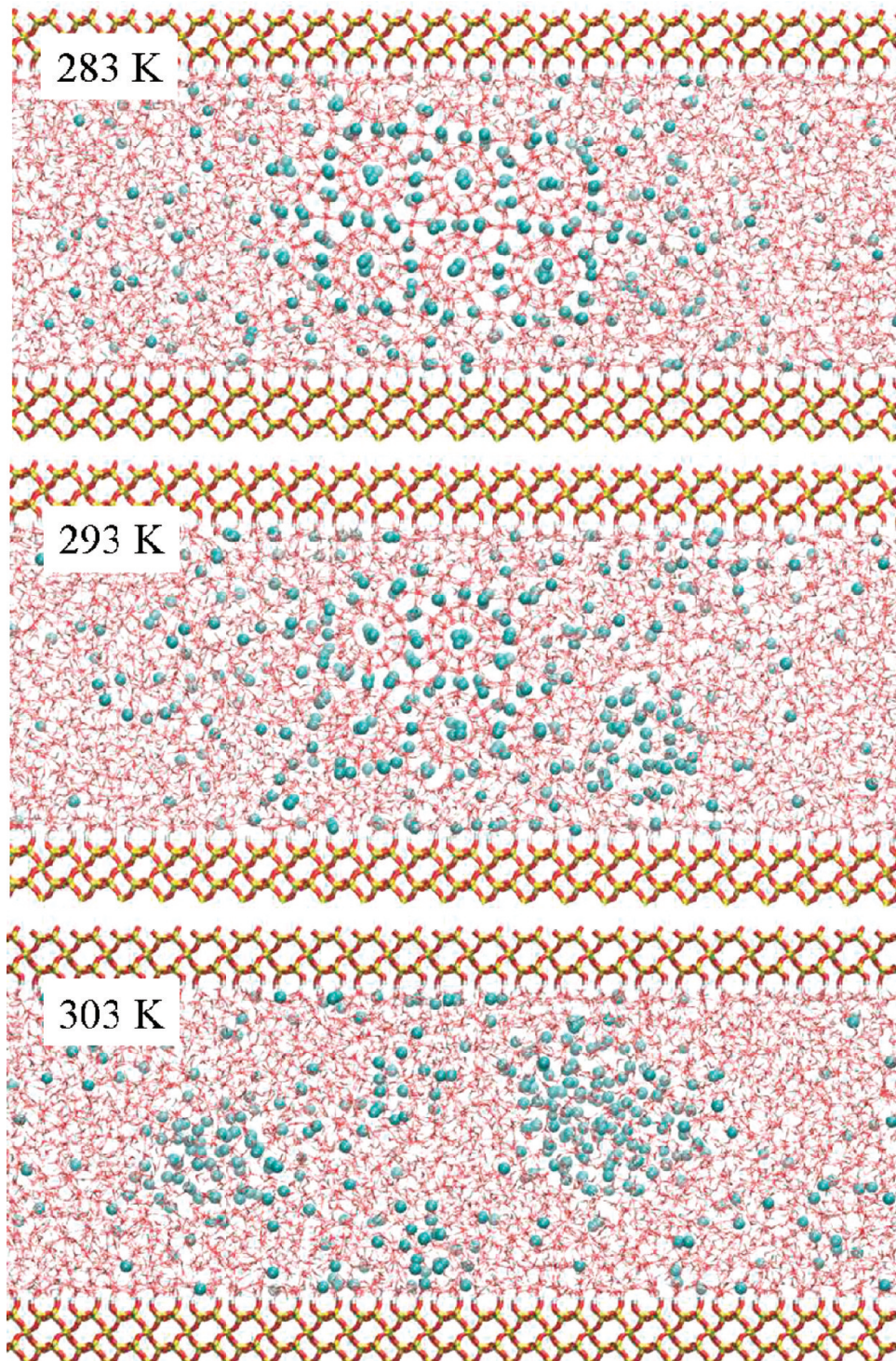


Figure 6. Simulation configurations at the end of the 2 ns NVE runs for decomposition of methane hydrate in the SWHW scenario at initial temperatures of 283, 293, and 303 K.

in Figure S5 and quantitatively in Figure S6 of the Supporting Information. The methane bubbles form to minimize the surface contact of the methane molecules with water and hydrophilic hydroxylated silica surface. In the SHW scenario, where the hydrate decomposes faster, the methane nanobubbles merge to a greater extent. At $t = 1.0$ ns there are three small nanobubbles at $z = -40$, -8 , and 15 Å. After 2 ns simulation time, these bubbles merge into two larger nanobubbles at $z = -30$ and 11 Å with approximate diameters

of 17 and 30 Å. The presence of these bubbles in the liquid phase may explain the “memory effect” as it has been shown experimentally that nanobubbles with radius of 50 nm constitute 600 cm^3 of gas per 1 dm^3 of water with internal pressures of up to 6 MPa.⁴² These nanobubbles persist for more than 2 weeks at atmospheric pressure and room temperature.⁴⁹ Previous simulation work^{13,20,50} also concluded that the memory effect is related to the high concentration of

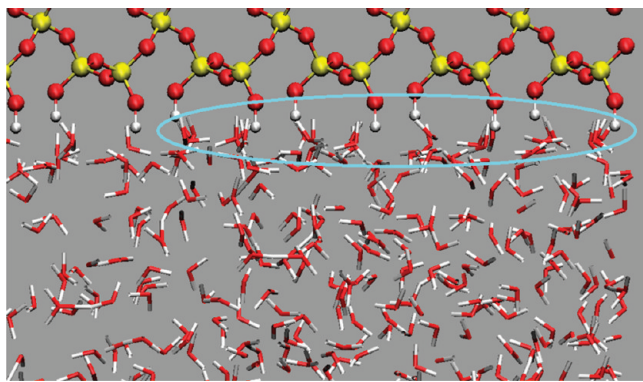


Figure 7. Snapshot of the surface configuration of the water molecules for a simulation at 303 K. The ordering of the water molecules near the hydroxylated silica surface is observed.

methane in the melt rather than the presence of hydrate structural precursors.

In sediments, heat conductance from the silica phase affects the rate of hydrate decomposition. In the present simulations, the silica phase was frozen, which leaves this boundary layer without thermal energy and furthermore unable to conduct heat. This is equivalent to assuming a small thermal conductivity for the silica phase. The experimental thermal conductivities of the materials important to these studies are given in Table 2. The thermal conductivity of the silica phase is between that of ice and methane hydrate. Therefore, in sediments the silica phase can participate in the heat transfer process involved in the methane hydrate decomposition. The sediments are usually in the form of sandstone or other granular silica, which can affect the value of their thermal conductivity. In these simulations, we observed that the presence of the silica surface enhances the hydrate decomposition rate. However, in the reservoirs, heat conductivity from

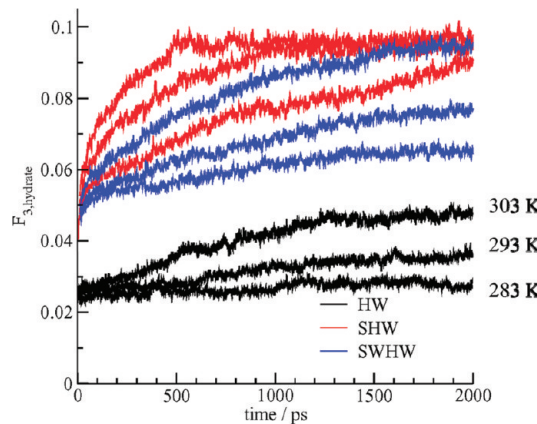


Figure 9. The average order parameter $F_{3,\text{hydrate}}$ of the hydrate phase at different temperatures for the HW, SHW, and SWHW scenarios at 283, 293, and 303 K.

Table 2. Experimental Thermal Conductivities of Phases Relevant to This Study

phase	thermal conductivity/W·K ⁻¹ ·m ⁻¹
SiO ₂	1.3–1.4
water	0.58 (at 0 °C)
ice	2.18 (at 0 °C)
methane hydrate	0.55–0.65 ^a

^aReferences 51 and 52.

the silica phase to the decomposing hydrate can also affect the rate of decomposition.

4. CONCLUSIONS

Methane hydrate decomposition under a confined geometry between two fully hydroxylated silica surfaces ~40 Å apart was

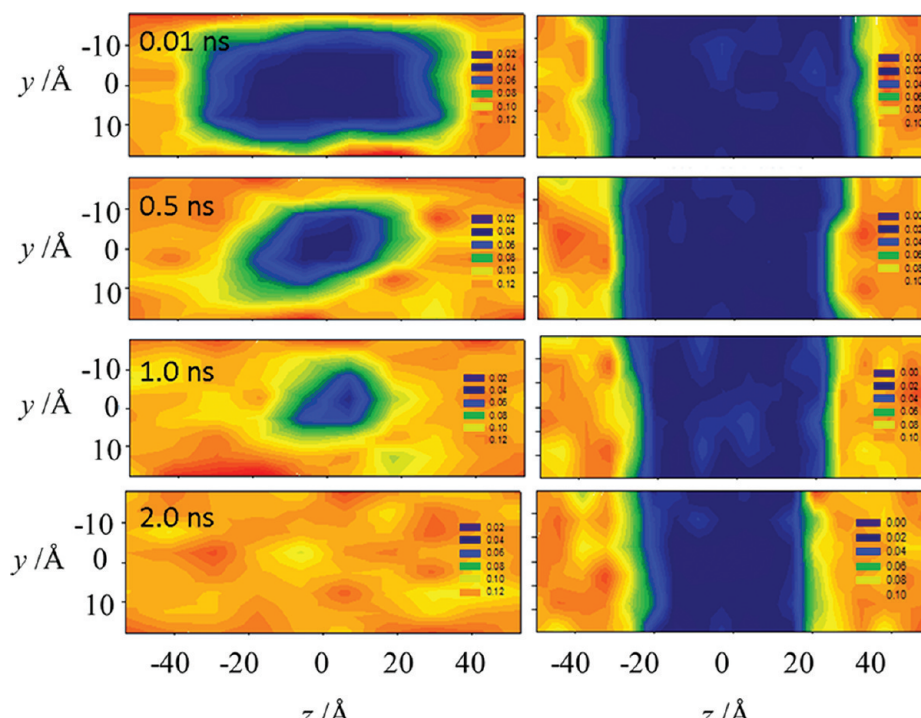


Figure 8. Contours of the local F_3 order parameter showing the dissociation trend under SWHW (left) and HW scenarios (right) at $T_{\text{init}} = 303$ K.

simulated with molecular dynamics in an NVE ensemble at initial temperatures of 283, 293, and 303 K to investigate the dissociation process closer to reservoir conditions. As expected, the rate of decomposition was lower at lower initial simulation temperatures. The dissociation rates in the presence of the silica surfaces were found to be faster than the nonconfined water-methane hydrate simulations. During hydrate dissociation, the hydrate core shrank in a stepwise manner with a curved decomposition front that extended between 5 and 8 Å. The presence of a water layer between the hydroxylated silica and methane hydrate alleviates the mismatch between the methane hydrate/hydroxylated silica lattices at the interface, and therefore, hydrate decomposed slower in the silica-water-hydrate-water (SWHW) scenario than the silica-water-hydrate (SWH) scenario. In both SWHW and SWH scenarios, the additional exposed surfaces made the methane hydrate decomposition faster for the hydrate-water (HW) scenario.

Labeling of water molecules revealed that there is exchange between water molecules from the surrounding liquid with the cages of the hydrate phase. This demonstrates the dynamic nature of the hydrate structure when it is in equilibrium with an aqueous phase and provides a mechanism for guest exchange between the liquid and hydrate phases.

■ ASSOCIATED CONTENT

Supporting Information

Details of the construction of the hydroxylated silica phase are shown in Figures S1 and S2. The pressure change in the simulations at different initial temperatures is given in Figure S3. The change of the F_3 order parameter for layers in the y -direction for the SHW and SWHW scenarios is shown in Figure S4. Snapshots of methane nanobubble formation after 2 ns for the three simulation scenarios are shown in Figure S5. The numbers of methane molecules along the z -axis for the three temperatures in each simulation are shown in Figure S6. The changes in the methane hydrate volume in the three scenarios with time are shown in Figure S7. This information is available free of charge via the Internet at <http://pubs.acs.org>.

■ AUTHOR INFORMATION

Corresponding Author

*E-mail: englezos@chbe.ubc.ca (P.E.), saman.alavi@nrc-cnrc.gc.ca (S.A.), and john.ripmeester@nrc-cnrc.gc.ca (J.A.R.).

Notes

The authors declare no competing financial interest.

■ ACKNOWLEDGMENTS

We acknowledge Natural Resources Canada (NRCan) under the program “Gas Hydrates as a Canadian Energy Alternative” for partial funding of this research. The financial support of the Natural Sciences and Engineering Research Council of Canada and the computational support from the National Research Council of Canada are gratefully acknowledged. We thank anonymous reviewers for comments.

■ REFERENCES

- (1) Davidson, D. W. In *Water: A Comprehensive Treatise*; Franks, F., Ed.; Plenum Press: New York, 1973; Vol. 2, p 115.
- (2) Englezos, P. *Ind. Eng. Chem. Res.* **1993**, *32*, 1251–1274.
- (3) Ripmeester, J. A. *Ann. N.Y. Acad. Sci.* **2000**, *912*, 1–16.
- (4) Sloan, E. D.; Koh, C. A. *Clathrate Hydrates of Natural Gases*, 3rd ed.; CRC Press: Boca Raton, FL, 2008.

- (5) Hester, K. C.; Brewer, P. G. *Annu. Rev. Mar. Sci.* **2009**, *1*, 303–327.
- (6) Holder, G. D.; Kamath, V. A.; Godbole, S. P. *Annu. Rev. Energy* **1984**, *9*, 427–445.
- (7) *Energy from Gas Hydrates: Assessing the Opportunities and Challenges for Canada*; The Council of Canadian Academies: Ottawa, Canada, 2008.
- (8) Committee on Assessment of the Department of Energy, Methane Hydrate Research and Development Program: Evaluating Methane Hydrate as a Future Energy Resource. *Realizing the Energy Potential of Methane Hydrate for the United States*; The National Academies Press: Washington, DC, 2010.
- (9) Ohgaki, K.; Takano, K.; Sangawa, H.; Matsubara, T.; Nakano, S. *J. Chem. Eng. Jpn.* **1996**, *29*, 478–483.
- (10) Baez, L. A.; Clancy, P. *Ann. N.Y. Acad. Sci.* **1994**, *715*, 177–186.
- (11) Rodger, P. M. *Ann. N.Y. Acad. Sci.* **1994**, *715*, 207–211.
- (12) Rodger, P. M.; Forester, T. R.; Smith, W. *Fluid Phase Equilib.* **1996**, *116*, 326–332.
- (13) Rodger, P. *Ann. N.Y. Acad. Sci.* **2000**, *912*, 474–482.
- (14) Yasuoka, K.; Murakoshi, S. *Ann. N.Y. Acad. Sci.* **2000**, *912*, 678–684.
- (15) Tse, J. S.; Klug, D. D. *J. Supramol. Chem.* **2002**, *2*, 467–472.
- (16) Moon, C.; Taylor, P. C.; Rodger, P. M. *Can. J. Phys.* **2003**, *81*, 451–457.
- (17) English, N. J.; MacElroy, J. M. D. *J. Chem. Phys.* **2004**, *120*, 10247.
- (18) English, N. J.; Johnson, J. K.; Taylor, C. E. *J. Chem. Phys.* **2005**, *123*, 244503.
- (19) Ding, L. Y.; Geng, C. Y.; Zhao, Y. H.; Wen, H. *Mol. Simul.* **2007**, *33*, 1005–1016.
- (20) Hawtin, R. W.; Quigley, D.; Rodger, P. M. *Phys. Chem. Chem. Phys.* **2008**, *10*, 4853–4864.
- (21) English, N. J.; Phelan, G. M. *J. Chem. Phys.* **2009**, *131*, 074704.
- (22) Myshakin, E. M.; Jiang, H.; Warzinski, R. P.; Jordan, K. D. *J. Phys. Chem. A* **2009**, *113*, 1913–1921.
- (23) Walsh, M. R.; Koh, C. A.; Sloan, E. D.; Sum, A. K.; Wu, D. T. *Science* **2009**, *326*, 1095.
- (24) Alavi, S.; Ripmeester, J. A. *J. Chem. Phys.* **2010**, *132*, 144703.
- (25) Iwai, Y.; Nakamura, H.; Arai, Y.; Shimoyama, Y. *Mol. Simul.* **2010**, *36*, 246–253.
- (26) Ripmeester, J. A.; Alavi, S. *ChemPhysChem* **2010**, *11*, 978–980.
- (27) Sarupria, S.; Debenedetti, P. G. *J. Phys. Chem. A* **2011**, *115*, 6102–6111.
- (28) Bagherzadeh, S. A.; Englezos, P.; Alavi, S.; Ripmeester, J. A. *J. Chem. Thermodyn.* **2011**, *44*, 13–19.
- (29) Riedel, M.; Collet, T.; Malone, M.; Akiba, F.; Blanc-Valleron, M.; Ellis, M.; Guerin, G.; Hashimoto, Y.; Heuer, V.; Higashi, Y.; Holland, M.; Jackson, P.; Kaneko, M.; Kastner, M.; Kim, J.-H.; Kitajima, H.; Long, P.; Malinverno, A.; Myers, G.; Palekar, L.; Pohlman, J.; Schultheiss, P.; Teichert, B.; Torres, M.; Tréhu, A.; Wang, J.; Wortmann, U.; Yoshioka, H. *EOS, Trans. Am. Geophys. Union* **2006**, *87*, 325.
- (30) Bai, D.; Chen, G.; Zhang, X.; Wang, W. *Langmuir* **2011**, *27*, 5961–5967.
- (31) Liang, S.; Rozmanov, D.; Kusalik, P. G. *Phys. Chem. Chem. Phys.* **2011**, *13*, 19856–19864.
- (32) Smith, W.; Forester, T. R. *DL_POLY_2*; STFC Daresbury Laboratory, 2009.
- (33) Martin, M. G.; Siepmann, J. I. *J. Phys. Chem. B* **1998**, *102*, 2569–2577.
- (34) Berendsen, H. J. C.; Grigera, J. R.; Straatsma, T. P. *J. Phys. Chem.* **1987**, *91*, 6269–6271.
- (35) Lopes, P. E. M.; Murashov, V.; Tazi, M.; Demchuk, E.; MacKerell, A. D. Jr. *J. Phys. Chem. B* **2006**, *110*, 2782–2792.
- (36) Levien, L.; Prewitt, C. T.; Weidner, D. J. *Am. Mineral.* **1980**, *65*, 920.
- (37) Luis, D. P.; López-Lemus, J.; Mayorga, M.; Romero-Salazar, L. *Mol. Simul.* **2010**, *36*, 35–40.
- (38) Conde, M. M.; Vega, C. J. *Chem. Phys.* **2010**, *133*, 064597.

- (39) Handa, Y. P.; Zakrzewski, M.; Fairbridge, C. *J. Phys. Chem.* **1992**, *96*, 8594–8599.
- (40) Clennell, M. B.; Hovland, M.; Booth, J. S.; Henry, P.; Winters, W. *J. J. Geophys. Res.* **1999**, *104*, 22985–23004.
- (41) Vatamanu, J.; Kusalik, P. G. *J. Phys. Chem. B* **2006**, *110*, 15896–15904.
- (42) Argyris, D.; Tummala, N. R.; Striolo, A.; Cole, D. R. *J. Phys. Chem. C* **2008**, *112*, 13587–13599.
- (43) Totland, C.; Steinkopf, S.; Blokhus, A. M.; Nerdal, W. *Langmuir* **2011**, *27*, 4690–4699.
- (44) Anderson, A.; Ashurst, W. R. *Langmuir* **2009**, *25*, 11549–11554.
- (45) Handa, Y. P.; Stupin, D. Y. *J. Phys. Chem.* **1992**, *96*, 8599–8603.
- (46) Henry, P.; Thomas, M.; Clennell, M. B. *J. Geophys. Res.* **1999**, *104*, 23005–23022.
- (47) Wilder, J. W.; Smith, D. H.; Seshadri, K. *Langmuir* **2001**, *17*, 6729–6735.
- (48) Uchida, T.; Ebinuma, T.; Takeya, S.; Nagao, J.; Narita, H. *J. Phys. Chem. B* **2002**, *106*, 820–826.
- (49) Ohgaki, K.; Khanh, N. Q.; Joden, Y.; Tsuji, A.; Nakagawa, T. *Chem. Eng. Sci.* **2010**, *65*, 1296–1300.
- (50) Vatamanu, J.; Kusalik, P. G. *Phys. Chem. Chem. Phys.* **2010**, *12*, 15065.
- (51) Waite, W. F.; Stern, L. A.; Kirby, S. H.; Winters, W. J.; Mason, D. H. *Geophys. J. Int.* **2007**, *169*, 767–774.
- (52) Huang, D.; Fan, S. *J. Chem. Eng. Data* **2004**, *49*, 1479–1482.